Available online at www.sciencedirect.com

jmr&t Journal of Materials Research and Technology

journal homepage: www.elsevier.com/locate/jmrt

Original Article

Study of direct aging heat treatment of additively manufactured PH13–8Mo stainless steel: role of the manufacturing process, phase transformation kinetics, and microstructure evolution

FNU Md Moniruzzaman [a], *Shawkat Imam Shakil* [b], *Sugrib Kumar Shaha* [c], *Josh Kacher* [c], *Ali Nasiri* [d], *Meysam Haghshenas* [b], *Amir Hadadzadeh* [a,*]

[a] *Department of Mechanical Engineering, University of Memphis, Memphis, TN, USA*
[b] *Department of Mechanical, Industrial and Manufacturing Engineering, University of Toledo, Toledo, OH, USA*
[c] *School of Materials Science and Engineering, Georgia Institute of Technology, GA, USA*
[d] *Department of Mechanical Engineering, Dalhousie University, Halifax, Canada*

ARTICLE INFO

Article history:
Received 6 February 2023
Accepted 5 April 2023
Available online 8 April 2023

Keywords:
Additive manufacturing
PH13–8Mo stainless Steel
Phase transformation
Precipitation hardening
Strength-ductility trade-off

ABSTRACT

Direct aging heat treatment recipes were developed for additively manufactured (AM) PH13–8Mo stainless steel by studying the kinetics of precipitation phase transformation in the as-built material. The samples were printed using two AM processes; *i.e.*, arc-directed energy deposition (arc-DED) and laser-powder bed fusion (L-PBF) techniques. The as-built samples were characterized using differential scanning calorimetry (DSC) to determine the characteristics of precipitation phase transformation. Due to different thermal histories during the arc-DED and L-PBF processes, the resulting microstructures and physical properties were different; therefore, the precipitation kinetics were different. The kinetics results were used to design a direct aging heat treatment to promote the formation of β-NiAl precipitates. Two different heat treatment recipes were designed considering the differences between the two materials. Direct aging of arc-DED-PH13-8Mo resulted in a concurrent improvement in strength and ductility, while direct aging of L-PBF-PH13-8Mo resulted in a significant increase in strength and retention of ductility. The microstructure was then correlated to the physical (*i.e.*, the kinetics of precipitation) and mechanical (*i.e.*, strength and ductility) properties. Concurrent strength and ductility improvement in the arc-DED-PH13-8Mo was controlled by the evolution of nano-scaled β-NiAl clusters. In the L-PBF-PH13-8Mo, the strength enhancement was governed by the evolution of nano-scaled β-NiAl precipitates, while the ductility retention was dictated by preserving the pre-existing dislocation networks.

* Corresponding author.
E-mail address: amir.hadadzadeh@memphis.edu (A. Hadadzadeh).
https://doi.org/10.1016/j.jmrt.2023.04.023

Nomenclatures and abbreviations

$\Delta\sigma_c$	Strength increment due to coherency strengthening
$\Delta\sigma_{sb}$	Strength increment due to sub-boundary hardening
$\Delta\sigma_m$	Strength increment due to modulus mismatch hardening
$\Delta\sigma_o$	Strength increment due to order strengthening
$\Delta\sigma_p$	Strength increment due to precipitation hardening
γ_{APB}	Anti-phase boundary energy
λ_m	Martensite lath size
ρ_d	Dislocation density
ΔG	Shear modulus mismatch
AM	Additive manufacturing
APB	Anti-phase boundary
ASTM	American Society for Testing and Material
BF	Bright filed
DED	Directed energy deposition
DSC	Differential scanning calorimetry
EBSD	Electron backscatter diffraction
ER	Elastic recovery
EDS	Energy-dispersive X-ray spectroscopy
E_r	Reduced modulus
f	Volume fraction
FIB	Focused ion beam
HRC	Rockwell C hardness
IPF	Inverse pole figure
ISO	International Organization for Standardization
L-PBF	Laser-powder bed fusion
OM	Optical microscope
PI	Plasticity index
SAED	Selected area electron diffraction
SEM	Scanning electron microscope
STEM	Scanning transmission electron microscope
TEM	Transmission electron microscope
TS	Tensile strength
YS	Yield strength
G	Shear modulus
M	Taylor factor
b	Burgers vector
r	Precipitate radius
ε	Lattice mismatch parameter

1. Introduction

Martensitic precipitation hardenable (PH) stainless steels exhibit a broad range of attractive properties, such as ultra-high strength, good ductility, and adequate corrosion resistance, which make them suitable for various applications, including structural parts for aircraft, nuclear power plants, marine vessels, and petrochemical plants [1]. The microstructure of these steels consists of a low-carbon and ductile martensitic matrix and nano-scale intermetallics that contribute to the strengthening of the alloys [2]. The typical precipitates in the maraging stainless steels include Cu-rich, β-NiAl, Ni_3Ti, and Ni_3Al intermetallics [3], depending on the chemistry of the material. PH stainless steels are available in a variety of commercial grades, such as 17–4 PH, 15–5 PH, 17–7 PH, and PH13–8Mo [4,5]. They vary significantly with regard to their microstructural characteristics, mechanical properties, resistance to corrosion, applications, and production costs [5,6]. Among these steels, PH13–8Mo has superior mechanical characteristics compared to other types of PH steels [7]. PH13–8Mo stainless steel is hardened by the evolution of ordered intermetallic NiAl precipitates that have a structure similar to that of CsCl [8], developed during an aging heat treatment [9].

Despite the attractive mechanical characteristics of PH stainless steels, they suffer from poor machinability and formability, leading to their costly and time-consuming production through traditional fabrication techniques [10]. Additive manufacturing (AM) is a potential alternative route for the fabrication of PH stainless steel parts due to its capability to fabricate on-demand and custom parts. Due to the emerging developments in the AM sector and its widespread adoption in various industries [11–13], it is essential to study the additive manufacturing of PH stainless steels. Among the available AM processes, laser-powder bed fusion (L-PBF) and arc-directed energy deposition (arc-DED) technologies have been widely used to fabricate PH stainless steels [6,14–16]. In the L-PBF process, successive layers of powder feedstock material are melted and joined on top of each other using a laser beam as the heat source to create the components. This technique allows the manufacturing of complex and near-net-shaped geometries with superior mechanical properties [11]. On the other hand, in the arc-DED process, an electric arc is used as the heat source to melt and join successive layers of feedstock wire [17]. Due to its higher material deposition rates compared to other AM techniques, arc-DED can manufacture large-scale parts [16]. In general, L-PBF is suitable for fabricating relatively small and complex components with fine microstructures and surface finishes, while arc-DED is a more cost-effective manufacturing technique for the production of large-scale components with relatively simple designs.

Understanding the evolution of hierarchical micro and nano-scale features during the L-PBF and arc-DED processes is essential to developing comprehensive processing-microstructure-property relationships for AM-PH13-8Mo. In particular, the evolution of hardening precipitates is crucial since they act as the main strengthening mechanism. In the case of L-PBF-PH13-8Mo, the recommended heat treatment procedure consists of a solutionizing treatment step (typically 850–1010 °C for 0.5–1 h) followed by aging at 525–530 °C for 2–4 h [18]. This heat treatment recipe is recommended by EOS GmbH for the as-printed CX stainless steel (compositionally equivalent to PH13–8Mo) processed through L-PBF [19]. It appears from the literature (as summarized in [18]) that all researchers have been using the same recipe regardless of their adopted process parameters, sample geometry, orientation, etc. On the other hand, during the aging of arc-DED-PH13-8Mo at elevated temperatures (600 °C), β-NiAl precipitates were observed along with the carbides in the martensitic laths [14]. In addition, Ghaffari et al. [6] reported that δ-ferrite and retained austenite were seen in the as-built arc-DED-PH13-

8Mo sample. In a later study, they reported that solutionizing at 1050 °C followed by 4 h of isothermal aging at 500 °C resulted in an increase in strength (from 1117 MPa to ~1510 MPa) and a drop in elongation (from 11.5% to 9.5%). They also found β-NiAl precipitates in the heat-treated sample of arc-DED-PH13-8Mo [6,20].

Considering the available literature, it appears that the heat treatment of L-PBF and arc-DED PH13–8Mo steel has been developed by adopting either the recommended recipes or a trial-and-error method. On the other hand, the majority of adopted heat treatments include a high-temperature solutionizing step. It is well understood that the microstructure of AM steels consists of hierarchical features spanning orders of magnitude [21]. These features contribute to the strength and ductility of the alloy through distinct mechanisms. Therefore, it is beneficial to preserve them during heat treatment. Low-temperature direct aging could potentially retain the formed microstructural features in the as-printed condition. In this study, PH13–8Mo stainless steel samples were fabricated using L-PBF and arc-DED processes. Since the samples experienced different thermal histories and cooling conditions, substantially different microstructural features were attained. Therefore, the physical properties and specifically the kinetics of precipitation were expected to be different. To elaborate on these differences, the precipitation kinetics were studied using differential scanning calorimetry (DSC). Using the kinetics models, direct aging heat treatments were designed for the targeted alloy processed through both AM methods. The microstructure was then correlated to the mechanical properties. It should be noted that the purpose of the heat treatment design in the current study was to evaluate the quasi-static tensile properties. While small defects like porosities are inherent to the fusion-based AM processes [22,23] that can affect fatigue behavior, we did not evaluate the effect of our heat treatment on the defect-fatigue relationship.

2. Materials and methods

2.1. AM processes

The arc-DED walls of PH13–8Mo with dimensions of 110 mm (width) × 90 mm (height) × 6.5 mm (thickness) were printed using a 6-axis Fanuc robot equipped with a GMA torch and Lincoln Electric's S-350 Power Wave power source. The feedstock used to build the walls was PH13–8Mo wire with a diameter of 1.143 mm and a nominal chemical composition shown in Table 1 [24]. The process parameters included a scanning speed of 4 mm/s, an arc current of 135 A, an arc voltage of 28 V, and a wire feeding speed of 67 mm/s. Each deposited layer had an approximate height of 5 mm and to maintain consistency a back-and-forth scanning approach was employed.

An EOS M290 machine was employed to print cylindrical rods of PH13–8Mo using the L-PBF technique. The nominal composition of the PH13–8Mo powder is shown in Table 1 [25]. The average particle size was 37.5 μm ± 16 μm. The rods had a diameter of 12 mm and a length of 120 mm and were printed using the process parameters recommended by the EOS. The key process parameters included laser power ($P = 258.7$ W), scan speed ($\upsilon = 1067$ mm/s), hatch distance ($h = 100$ μm), and layer thickness ($l = 30$ μm). The laser spot size was 100 μm. The printing was completed using a stripe scanning strategy where the laser beam rotated 67° between the successive layers.

Table 1 – Nominal composition of the feedstock wire and powder.

	Composition (wt.%)					
	Cr	Ni	Al	Mo	C	Fe
Wire feedstock (arc-DED)	12.75	8.0	1.13	2.25	0.05	Bal.
Powder feedstock (L-PBF)	12	9.2	1.6	1.4	0.05	Bal.

To conduct further thermal, mechanical, and microstructural analyses, the samples were extracted from the middle of the DED wall and PBF rods, away from the bottom and top to ensure microstructural and chemical consistency and homogeneity. In specific, the first and last two layers in the DED and the first and last 33 layers in the PBF parts were excluded from these analyses.

2.2. DSC analysis and heat treatment

To conduct DSC analysis, the samples were machined into small disks with a diameter of 4 mm and a height of 2 mm to maintain consistency throughout all analyses. The disks were machined from different height positions (excluding the first and last layers as mentioned previously) to achieve a representative material behavior. SDT 650-TA (Delaware, USA) instrument was used to measure the thermal profiles of the samples during continuous heating from room temperature to 1000 °C. The samples were heated at heating rates of 20–50 °C/min. To avoid oxidation, DSC tests were carried out with an argon shielding gas flowing continuously at a rate of 100 mL/min. The heat flow data were measured and used to determine the kinetics of precipitation phase transformations. The kinetics of phase transformation results were employed to determine the temperature and time required for the direct aging of each set of samples. The heat treatments were conducted in a Lindberg Blue M tube furnace by Thermo Scientific.

2.3. Mechanical testing

A Wilson Rockwell hardness tester with a diamond indenter under 150 kg. *f* load was used to measure the macro-hardness of the as-built and heat-treated specimens. The arc-DED-PH13-8Mo hardness test specimens were 6.5 mm by 6.5 mm by 3 mm in size whereas the L-PBF-PH13-8Mo samples were 12 mm in diameter and 3 mm in height.

Depth-sensing nanoindentation tests were conducted on all samples employing a self-similar pyramidal diamond Berkovich indenter with a tip radius of 100 nm. Standard ISO 14577 constant loading rate indentation method was utilized with 200 mN peak load, 10 mN/s loading rate, and 5 s of dwell time (holding time at peak load). A 5 × 5 array of indents was performed on each sample to make sure the repeatability of the results. The indentation hardness (H_{ind}) of the samples was determined using Eq. (1) [26].

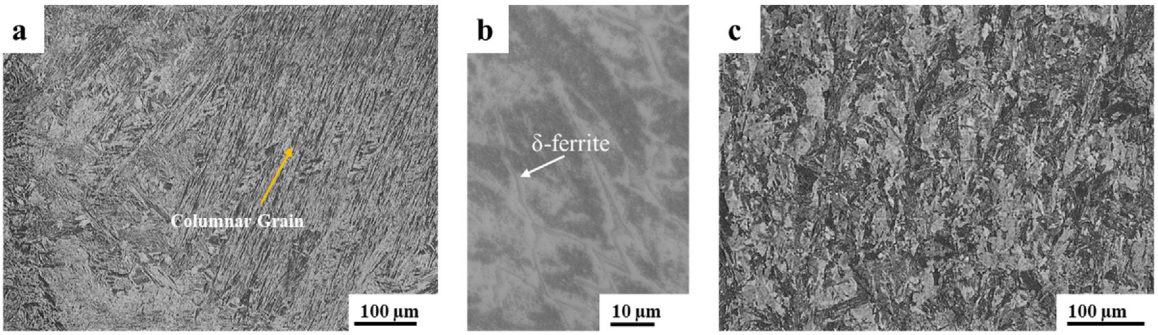

Fig. 1 – OM images of as-built (a) and (b) arc-DED-PH13-8Mo, and (c) L-PBF-PH13-8Mo.

$$H_{ind} = \frac{P}{24.5(h + 0.06R)^2} \quad (1)$$

where P is the indentation load (mN), h is the indentation depth (nm), and R is the indenter tip radius (100 nm for the current study).

Using the indentation results, some in-service performance indicators (indexes) of the material could be evaluated, including the indentation hardness (H or H_{ind}) and reduced modulus (E_r). One of these indicators is the hardness-to-reduced modulus ratio $\left(\frac{H}{E_r}\right)$, which represents the wear resistance of the material [27]. While hardness has always been thought of as the major attribute of a material that defines wear resistance, there is compelling evidence that the elastic modulus can also have a significant impact on wear behavior. Multiple authors [28–30] have demonstrated that the ability to resist elastic strain to failure, which is related to the hardness/elastic modulus (or reduced modulus from nanoindentation) ratio $\left(\frac{H}{E_r}\right)$, is a better measure for predicting wear resistance than hardness alone. With a high $\frac{H}{E_r}$ ratio, the material will have a longer "elastic strain to failure" which will allow the applied load to be distributed over a larger area, and as such, delay the onset of plastic deformation or wear-related failure [29]. Another indicator is the yield pressure $\left(\frac{H^3}{E_r^2}\right)$ in MPa, representing the resistance to plastic deformation [27]. The indentation results were also analyzed toward understanding the mechanical behavior of the materials in terms of the plasticity index (PI) and elastic recovery (ER) during the

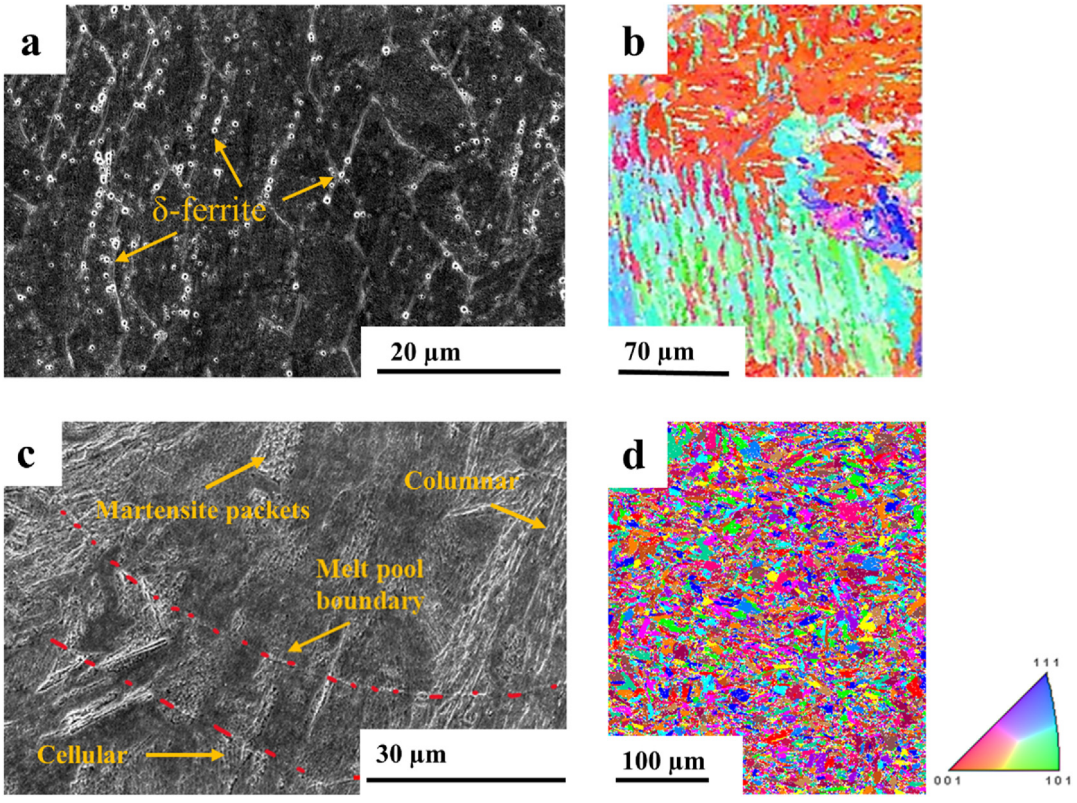

Fig. 2 – (a) SEM micrograph and (b) EBSD-IPF maps of as-built arc-DED-PH13-8Mo, and (c) SEM image and (d) EBSD-IPF of as-built L-PBF-PH13-8Mo.

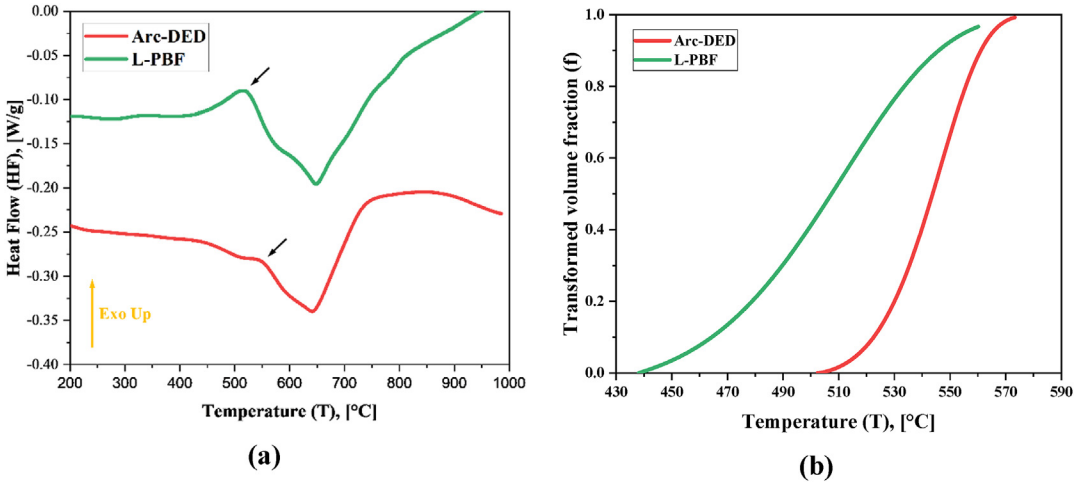

Fig. 3 – (a) The representative DSC curves and (b) volume fraction of transformed precipitates in arc-DED-PH13-8Mo and L-PBF-PH13-8Mo at 20 °C/min. The black arrows show the exothermic precipitation peak.

deformation process. The *PI* and *ER* values represent the plastic and elastic portion of the total work done by the indenter. *PI* and *ER* are unique functions of $\left(\frac{H}{E_r}\right)$ and the relation is given by $\left(PI = 1 - ER = 5\left(\frac{H}{E_r}\right)\right)$ [31]. While the plasticity index relates to the intrinsic plasticity or formability of an alloy, the elastic recovery measures the amount of energy released from an alloy after being loaded and demonstrates its resilience to impact loading [30].

In addition, tensile tests were carried out using the Shimadzu AGS-X series, a universal tabletop testing machine. The load and displacement data were recorded by the TRAPEZIUMX software. A digital extensometer was employed to observe the change in the gauge length of the samples. The dog-bone-shaped samples were cut from the arc-DED-PH13-8Mo wall and L-PBF-PH13-8Mo rods following the ASTM E8/E8M-21. The gauge diameter was 2.5 mm, and its height was 10 mm. For the samples with higher strength, a TestResources tensile machine with a load capacity of 50 kN was used. The displacement was measured using a clip-on miniature transversal diametral extensometer.

2.4. *Microstructural characterization*

OM, SEM, EBSD, and TEM analyses were performed to examine the microstructures of arc-DED-PH13-8Mo and L-PBF-PH13-8Mo specimens in the as-built and heat-treated conditions. The sample preparation for the OM, SEM, and EBSD characterizations included a standard metallography procedure. OM and SEM samples were etched with Fry's reagent. A Leica DM2700 M microscope was used for taking OM images, while an FEI-Nova NanoSEM (FE-SEM) was used for SEM imaging. The EBSD analysis was performed using a Tescan MIRA3 scanning electron microscope (SEM) at an accelerating voltage of 20 kV.

With a Thermo Scientific Helios 5 UC DualBeam, thin films for TEM were prepared using the focused ion beam (FIB) lift-out approach. With an extreme field emission gun (X-FEG) source and a high tension adjustable from 80 to 200 kV, TEM studies were carried out using the Thermo Scientific Talos 200X. This system was configured with four in-column SDD Super-X detectors for energy-dispersive X-ray spectroscopy (EDS) signal detection and compositional mapping of the samples.

3. Results

3.1. *As-built microstructure*

OM micrographs of arc-DED and L-PBF-PH13-8Mo samples in the as-built condition are shown in Fig. 1. The arc-DED-PH13-8Mo exhibits a coarse columnar structure featured by residual δ-ferrite. Unidirectional heat flow during the solidification of the melt pools resulted in the epitaxial growth and evolution of columnar grains [32]. The mechanism of δ-ferrite formation has been previously discussed by Nemani et al. [14] and Ghaffari et al. [6]; the solidification started with the formation of δ-ferrite, followed by the subsequent solid-state phase transformations in steels. Due to the non-equilibrium cooling conditions, all δ-ferrite did not transform to austenite and part of that remained as a residual phase in the microstructure. On the other hand, the OM micrograph of the L-PBF-PH13-8Mo does not provide much information due to the ultrafine structure of the material. Such an ultrafine microstructure is inherent to the L-PBF process due to the ultrahigh cooling rates associated with the nature of the L-PBF [33].

Fig. 2 shows the SEM images and EBSD-inverse pole figure (IPF) maps of as-built arc-DED-PH13-8Mo and L-PBF-PH13-8Mo specimens. While δ-ferrite is seen in the SEM image of the arc-DED specimen, the SEM image of the L-PBF sample does not exhibit such a phase, which is consistent with the previous studies [34]. The reason that δ-ferrite did not evolve in the L-PBF sample is the slight difference between the chemical composition of the feedstock powder and wire used in this study, referring to Table 1. With a higher Ni content and lower Mo, the chromium-to-nickel equivalent ratio (Cr_{eq}/Ni_{eq}) in the powder feedstock changes, which will then affect the

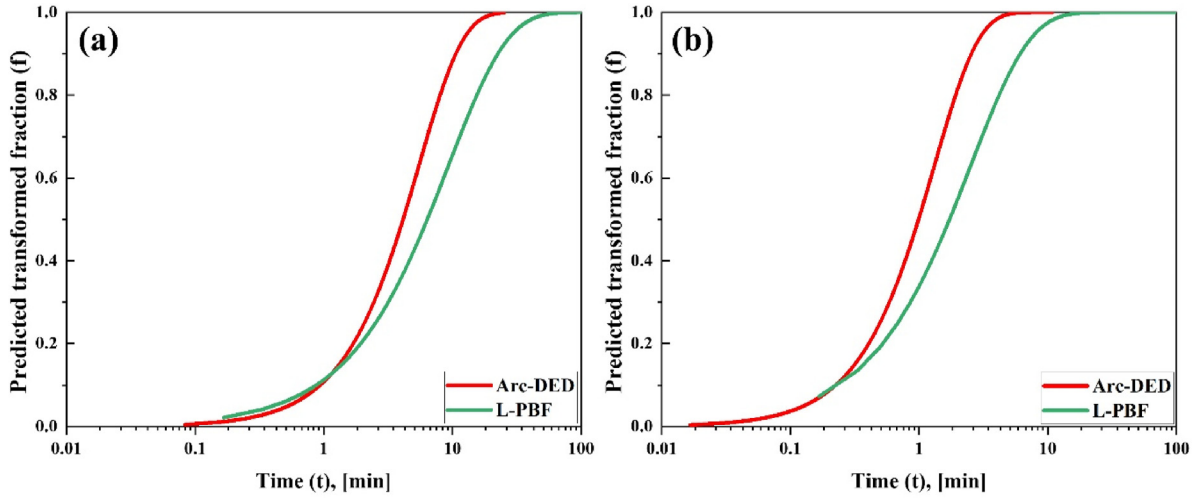

Fig. 4 – Modeled transformed volume fraction of precipitates in arc-DED-PH13-8Mo and L-PBF-PH13-8Mo at (a) 495 °C and (b) 550 °C.

solidification mode of the L-PBF-PH13-8Mo [35,36]. Due to substantial differences between the size of the melt pools in the two processes, while the melt pool boundaries are visible for the L-PBF sample, the SEM image of the arc-DED sample represents the microstructure of the material within a single pool. Some details of the columnar and cellular dendrites along with the martensite packets are seen in the micrograph of the L-PBF sample. Referring to the EBSD-IPF maps, it can be seen that the as-built arc-DED-PH13-8Mo exhibits an extremely coarse and columnar grain morphology whereas the as-built L-PBF-PH13-8Mo possesses a much finer grain structure. Both arc-DED and L-PBF-PH13-8Mo samples are composed of lath martensitic structures, where the martensite lath size (λ_m) is substantially different between the two materials. λ_m is 10.5 μm in the arc-DED and 1.9 μm in the L-PBF sample, representing almost an order of magnitude difference. The lath martensite was determined as the grain minor axis from the EBSD results.

3.2. *Kinetics of precipitation phase transformations*

Fig. 3 shows the representative DSC curves of the arc-DED and L-PBF-PH13-8Mo samples at a heating rate of 20 °C/min. Various exothermic and endothermic peaks are observed, each representing a specific solid-state phase transformation [37]. The peak of interest in this study is the exothermic peak (marked by an arrow) that is associated with precipitation. The DSC curves were processed and the fraction of transformed precipitates was determined using the method reported by Guo et al. [37]. Fig. 3 (b) shows the volume fraction of precipitation for non-isothermal heating with a heating rate of 20 °C/min for arc-DED and L-PBF-PH13-8Mo. It is observed that the precipitation onset temperature for arc-DED-PH13-8Mo is higher than that of the L-PBF-PH13-8Mo during non-isothermal heating, plausibly attributed to the processing-induced microstructural and physical properties variations between the materials. The precipitation onset temperature of arc-DED-PH13-8Mo is about 502 °C whereas, in the L-PBF-PH13-8Mo sample, the onset temperature is about 438 °C. However, the temperature range (438–560 °C; $\Delta T = 122$ °C) of precipitation process completion of L-PBF fabricated alloy is higher than that of its arc-DED counterpart (502–573 °C; $\Delta T = 71$ °C).

The volume fractions of transformed precipitates at different heating rates were employed to determine the activation energy for precipitation and kinetics of precipitation under both non-isothermal and isothermal heating

Table 2 – The desired set of aging temperatures and times for AM-PH13-8Mo, determined by the kinetics models.

Acronym	Fabrication Method	Aging temperature (°C)	Aging time (min)
DA-495-45	Arc-DED	495	45
DA-550-115	L-PBF	550	115

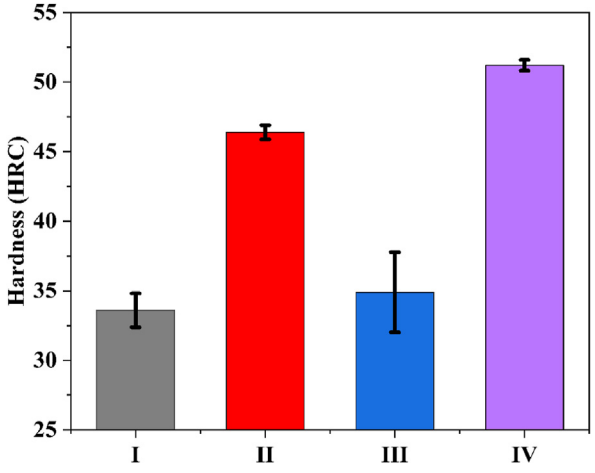

Fig. 5 – Comparison of the macro-hardness value of (I) as-built and (II) heat-treated arc-DED-PH13-8Mo, (III) as-built and (IV) heat-treated L-PBF-PH13-8Mo.

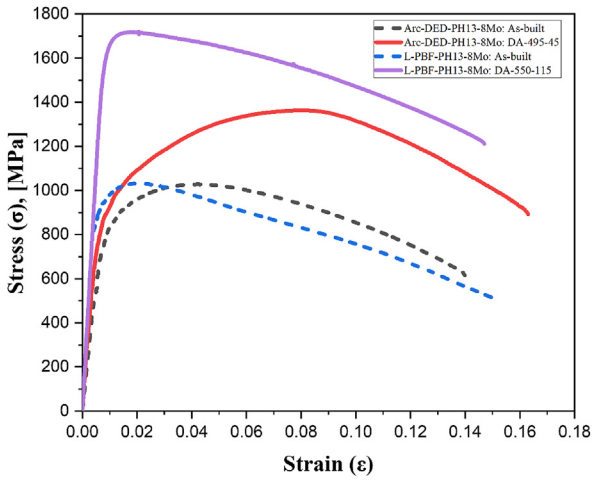

Fig. 6 – Stress-strain curves of arc-DED-PH13-8Mo and L-PBF-PH13-8Mo.

conditions [37]. The activation energy for precipitation in the arc-DED and L-PBF-PH13-8Mo was evaluated as 194 kJ/mol and 139 kJ/mol, respectively. The isothermal kinetics models were then used to determine the volume fraction of precipitates as a function of holding time under different isothermal heatings. Such modeling depicts direct aging; therefore, it was conducted for the range of onset to end temperatures of the precipitation peaks that appeared in the DSC curves (*i.e.*, 438–573 °C). Fig. 4 shows precipitation kinetics in the arc-DED and L-PBF-PH13-8Mo samples for isothermal aging at 495 °C and 550 °C. The difference in the kinetics of precipitation in the two samples stems from the substantial differences in the microstructures of the samples. Therefore, each sample should be heat treated using a distinct heat treatment recipe.

3.3. *Heat treatment and mechanical properties*

Using the precipitation kinetics models, the desired direct aging conditions for the arc-DED-PH13-8Mo were found to be at 495 °C with a hold time of 45 min (denoted by DA-495-45) whereas, for the L-PBF-PH13-8Mo, the desired direct aging temperature is 550 °C with a hold time of 115 min (denoted by DA-550-115), as observed in Table 2. The process of determining these conditions included direct aging of the samples at various temperatures with the holding times determined from the kinetics models. The hardness of the samples was then measured and used as a screening factor to determine the desired aging conditions. The conditions shown in Table 2 resulted in the maximum hardness of each material. The macro-hardness (HRC) values of the heat-treated samples using the recommended conditions in Table 2 are shown in Fig. 5. For the arc-DED-PH13-8Mo, the as-built specimen had an average macro-hardness of 33.6 ± 1.2 HRC, whereas the heat-treated specimen reached a hardness of 46.4 ± 0.5 HRC. On the other hand, the macro-hardness value of the as-built L-PBF sample has improved from 34.9 ± 2.9 HRC to 51.2 ± 0.4 HRC after aging treatment. The achieved hardness value of the heat-treated L-PBF-PH13-8Mo is higher than those reported previously, ascribed to the applied higher aging temperature in this study (i.e. 550 °C) as compared to that used by other researchers (typically in the range of 530 °C). Sun et al. [1] showed in their study that PH stainless steels are very sensitive to the aging temperature where a 20 °C deviation in the aging temperature can significantly affect the hardness and strength.

To further evaluate the effect of the recommended direct aging recipes on the mechanical performance of the AM-PH13-8Mo, uniaxial tensile tests were conducted on the as-built and heat-treated samples. The results are shown in Figs. 6 and 7. Interestingly, both tensile strength (TS) and ductility enhanced after the aging treatment of arc-DED-PH13-8Mo. Ductility improved from 14.0% to 16.3% with a slight rise in yield strength (YS) (from 860 MPa to 911 MPa) and a considerable increase in TS (from 1046 MPa to 1363 MPa). This differs from the available heat treatment procedures in literature which are commonly reported to improve the strength of arc-DED-PH13-8Mo at the expense of a reduction in ductility [6,14,20]. Therefore, the concurrent strength-ductility enhancement in this alloy is a unique finding of this study. Meanwhile, there are significant enhancements in YS and TS accompanied by a negligible ductility loss for L-PBF-PH13-8Mo. For this sample, the TS improved from 1032 MPa to

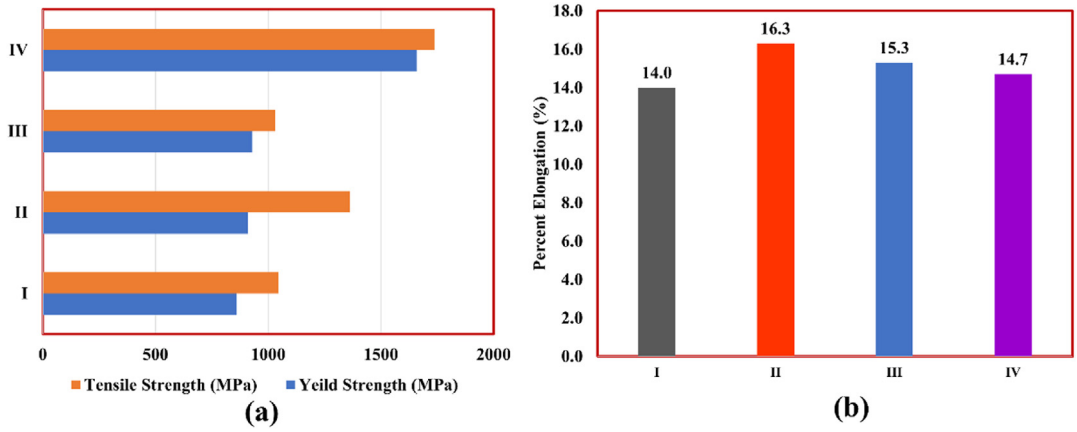

Fig. 7 – Comparisons of tensile properties of (I) as-built and (II) heat-treated arc-DED-PH13-8Mo, (III) as-built and (IV) heat-treated L-PBF-PH13-8Mo, (a) YS and TS, and (b) percent elongation.

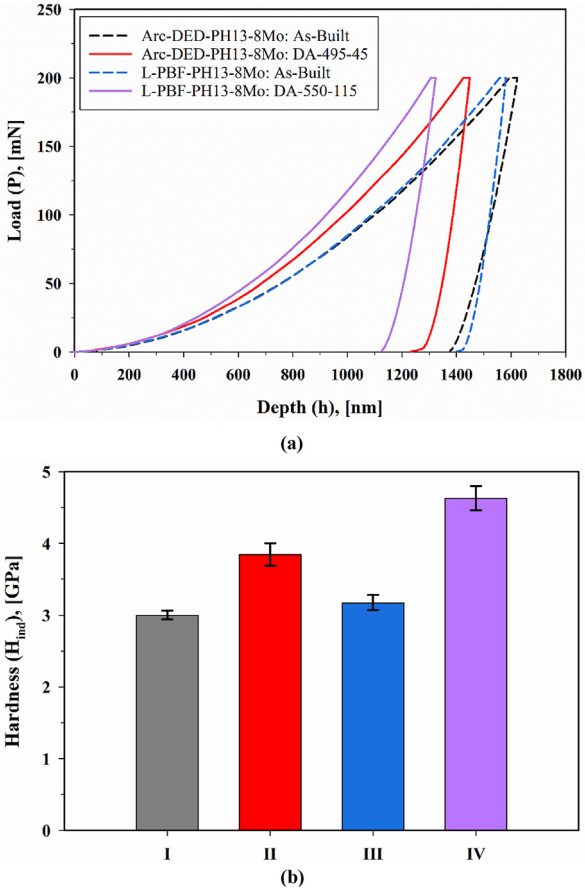

Fig. 8 – (a) Representative load-depth curves and (b) indentation hardness of (I) as-built and (II) heat-treated arc-DED-PH13-8Mo, (III) as-built and (IV) heat-treated L-PBF-PH13-8Mo.

1738 MPa, YS increased from 929 MPa to 1659 MPa, and ductility slightly decreased from 15.3% to 14.7% after applying the heat treatment parameters generated from the kinetics model. It should be noted that both the mechanical strength and ductility obtained by this study are superior to those of the manufacturer-suggested heat treatments [19].

In addition to the bulk-scale mechanical properties of the as-built and heat-treated AM-PH13-8Mo, the associated micro-mechanical response of the materials was also evaluated by employing a depth-sensing indentation testing technique (Figs. 8 and 9). Fig. 8 (a) shows the indentation-derived representative load-depth ($P-h$) curves of the samples. The indentation depth was measured for a constant load of 200 mN for all samples. Both as-built arc-DED and L-PBF-PH13-8Mo exhibit similar indentation depths, while the direct aging heat treatments significantly reduced the indentation depth, corresponding to the strengthening of the samples.

Fig. 8 (b) shows the indentation hardness (H_{ind}) of the samples. Similar to the trend observed in Fig. 5 for the microhardness of the samples, the as-built arc-DED and L-PBF-PH13-8Mo samples possess a close indentation hardness of 3.00 ± 0.06 GPa and 3.18 ± 0.11 GPa, respectively. The slightly higher hardness (both macro and micro) of the as-built L-PBF-PH13-8Mo is due to the finer microstructure of the material. Direct aging of the materials resulted in an indentation hardness of 3.85 ± 0.16 GPa in the arc-DED and 4.63 ± 0.17 GPa in the L-PBF sample.

The $\left(\frac{H}{E_r}\right)$ and $\left(\frac{H^3}{E_r^2}\right)$ ratios are ploted in Fig. 9 (a), displaying that the resistance to wear for the studied materials is in the same order as the hardness and strength. Large variations in the elastic property (*e.g.*, elastic modulus or reduced modulus) may affect wear resistance more than hardness and strength and therefore, the order of wear resistance might not always be the same as the order of hardness and strength.

Fig. 9 (b) reports the *PI* and *ER* values. The findings demonstrate that L-PBF materials with higher hardness have lower *PI* values than the softer arc-DED materials, and analogously, the harder heat-treated materials have lower *PI* values than the softer as-built materials. Higher *PI* means a lower elastic energy release potential and easier formability of the materials. The *ER* values, on the other hand, show that the studied materials are resistant to shock or impact loading in the order of their hardness. Since *ER* value reflects how much energy is released elastically from the material after being loaded, this parameter is particularly relevant in applications like impact loading.

3.4. *Microstructural evolution after heat treatment*

To investigate the effects of direct aging treatment on arc-DED-PH13-8Mo and L-PBF-PH13-8Mo microstructures, the DA-495-45 and DA-550-115 specimens were analyzed using OM, SEM, EBSD, and TEM.

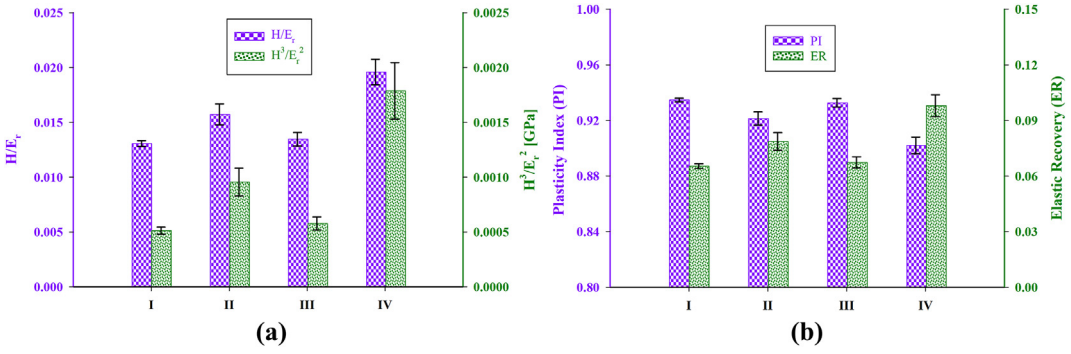

Fig. 9 – Indentation-derived properties of AM-PH13-8Mo: (a) $\frac{H}{E_r}$ and $\frac{H^3}{E_r^2}$ ratios, and (b) plasticity index and elastic recovery of (I) as-built and (II) heat-treated arc-DED-PH13-8Mo, (III) as-built and (IV) heat-treated L-PBF-PH13-8Mo.

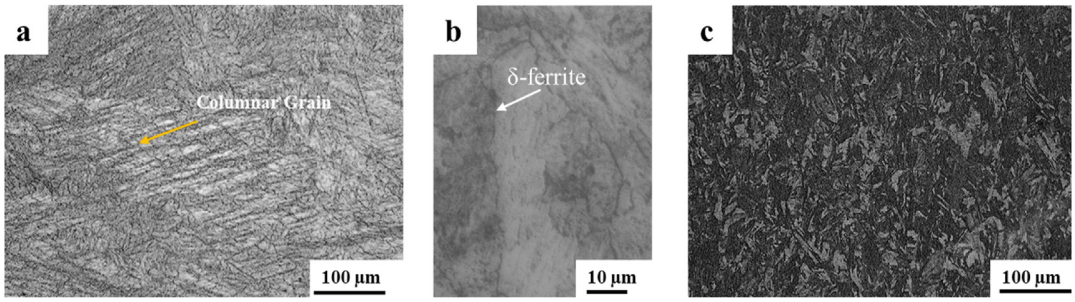

Fig. 10 – OM images of (a) and (b) arc-DED-PH13-8Mo: DA-495-45, and (c) L-PBF-PH13-8Mo: DA-550-115.

In the OM images of both DA-495-45 and DA-550-115 samples, no changes are observed as seen in Fig. 10. For the DA-495-45 specimen, columnar grains are visible at low magnification and δ-ferrite still exists in the microstructure. The low temperature of direct aging was not sufficient to eliminate the residual δ-ferrite, as it requires solutionizing at much higher temperatures (~1050 °C). On the other hand, similar grain morphology has been observed in DA-550-115 compared to the as-built condition (see Fig. 1(c) and Fig. 10 (c)).

The SEM results in Fig. 2 (as-built) and Fig. 11 (aged condition) do not reveal any significant differences. The morphology of the δ-ferrite, melt pool boundaries, columnar and cellular dendrites, and martensite packets remained almost the same as the as-built samples. The EBSD-IPF maps also seem very similar; however, to reveal the details of the characteristics, some important features were quantified. These features include the amount of austenite and martensite lath size (λ_m), as observed in Figs. 12 and 13. The austenite phase is either the one that did not transform to martensite during the solidification process or the one that evolved as a result of martensite decomposition during the heat treatment process. The former is known as retained austenite and the latter is known as reverted austenite [15]. The amount of retained austenite in the as-built arc-DED and L-PBF samples is 0.6% and 0.3%, respectively. After direct aging, no reverted austenite developed in the arc-DED sample while about 0.2% reverted austenite formed in the L-PBF sample. Nevertheless, the total retained/reverted austenite in both heat-treated samples is less than 1%, which has a negligible effect on the mechanical properties. On the other hand, direct aging heat treatment of AM-PH13-8Mo alloy resulted in the coarsening of martensite laths; λ_m increased from 10.5 μm to 19.9 μm in the arc-DED and from 1.9 μm to 2.1 μm in the L-PBF sample. Despite the lower aging temperature and time in the arc-DED sample, the rate of martensite coarsening was higher.

Fig. 14 and Fig. 15 show the FIB preparation along with bright field (BF) STEM images and diffraction patterns for the

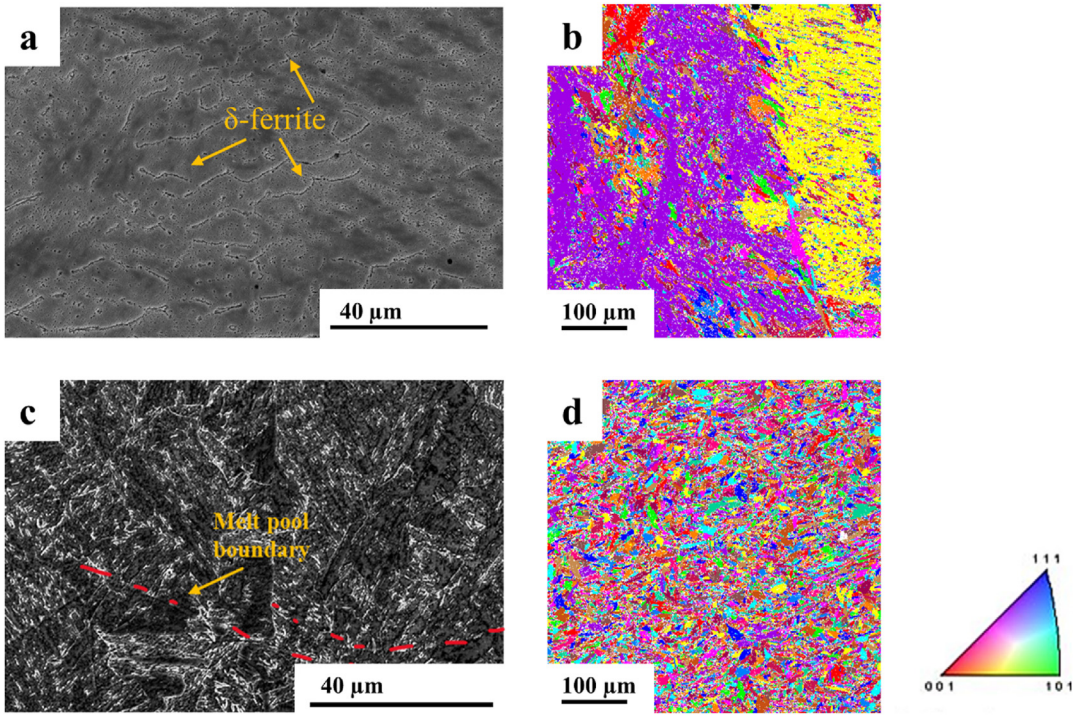

Fig. 11 – (a) SEM image and (b) EBSD-IPF map of DA-495-45, (c) SEM image, and (d) EBSD-IPF map of DA-550-115.

aged AM-PH13-8Mo samples. In both samples, the BF STEM images show a lath martensitic microstructure featured by entangled dislocation networks and small retained/reverted austenite phases. The existence of dislocations in the martensite matrix is a common phenomenon in both conventionally fabricated and AM martensitic steels [1,15]. These dislocations form during solidification under rapid cooling. Dislocation networks play an important role in both the strengthening and toughening of steels, so their preservation is crucial. Low-temperature heat treatments are more inclined to preserve dislocations rather than their annihilation. The dislocation density in the L-PBF sample is higher than that in the arc-DED sample, due to the substantially higher cooling rate in the former process [11].

The BF STEM image does not exhibit any observable β-NiAl precipitate, which is a common challenge in PH stainless steels [1]. To detect the β-NiAl precipitate structure, a diffraction pattern was obtained from the area indicated in the TEM-BF image of the sample, as shown in Fig. 14 (d) and Fig. 15(d), where weak superlattice reflections of nano-scale β-NiAl along with the matrix diffraction spots are visible. Comparing the arc-DED and L-PBF samples, it appears that the superlattice spots are weaker in the former material.

To reveal the nano-scale β-NiAl precipitates, STEM-EDS (energy dispersive X-Ray spectroscopy) was employed, and the results are shown in Fig. 16 for the arc-DED sample and Fig. 17 for the L-PBF sample. In the case of arc-DED-PH13-8Mo, the β-NiAl is in the form of nano-scale clusters rather than nano-scale precipitates. This could be a reason for the appearance of weaker superlattice spots in the SAED patterns of the arc-DED compared to the L-PBF sample. It appears that the absence of a solutionizing step is the main reason for such a phenomenon. Meanwhile, it appears that the evolution of the nano-scale clusters had a beneficial role in the concurrent enhancement of strength and ductility in the arc-DED sample. On the other hand, direct aging of L-PBF-PH13-8Mo resulted in the evolution of nano-scale precipitates, referring to Fig. 17. These precipitates are the main reason for the significant enhancement of strength in the material.

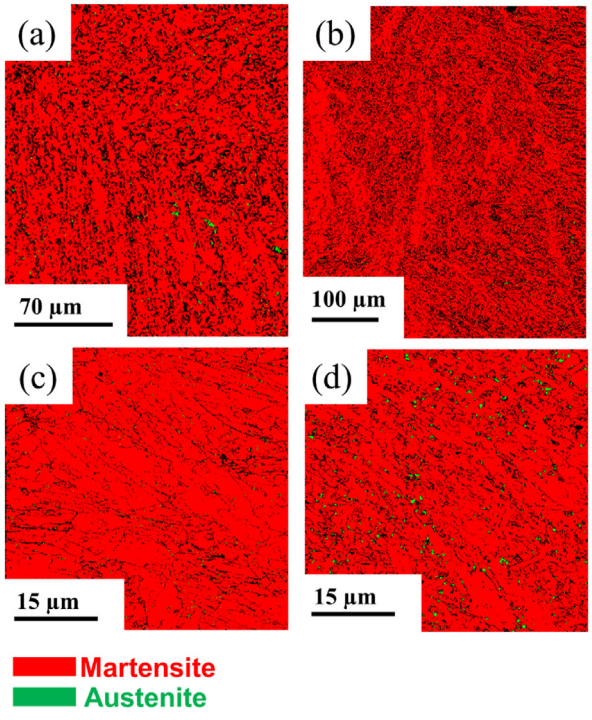

Fig. 12 – EBSD-phase maps of (a) as-built and (b) heat-treated arc-DED-PH13-8Mo, (c) as-built and (d) heat-treated L-PBF-PH13-8Mo.

4. Discussion

The fabrication of AM-PH13-8Mo stainless steel through two different AM techniques with substantial differences resulted in the evolution of two different microstructures. In specific, the cooling rate in the arc-DED process is in the order of 10^2–10^3 K/s [11,38] while in the L-PBF process is in the order of 10^3–10^8 K/s [33]. Therefore, a finer microstructure was evolved in the L-PBF-PH13-8Mo, where the martensite lath was an order of magnitude smaller than that in the arc-DED sample (1.9 μm vs. 10.5 μm). In addition, the dislocation density is higher in the L-PBF alloys due to the higher cooling rates [39]. Therefore, the strength of the as-built L-PBF-PH13-8Mo is higher than the arc-DED-PH13-8Mo; YS = 929 MPa vs. 860 MPa and TS = 1659 MPa vs. 911 MPa. The main strengthening mechanisms in the PH martensitic steels include sub-boundary hardening ($\Delta\sigma_{sb}$), dislocation hardening ($\Delta\sigma_d$), and precipitation hardening ($\Delta\sigma_p$) mechanisms [40]. In the as-built sample (in the absence of the precipitates), the governing mechanisms are sub-boundary hardening and dislocation hardening. The sub-boundary hardening is associated with the martensite laths, where the laths boundaries impede the dislocation motion similar to the Hall-Petch effect. The strength increment due to the sub-boundary hardening is expressed as [40],

$$\Delta\sigma_{sb} = 10Gb/\lambda_m \quad (2)$$

where G is the shear modulus of the matrix and b is the Burgers vector. Considering the martensite lath size in the samples (λ_m), the sub-boundary strength increment in the L-PBF-PH13-8Mo is 5.5 times than that in the arc-DED-PH13-

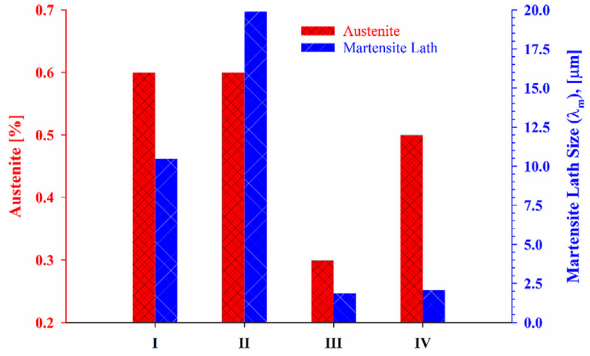

Fig. 13 – Austenite amount and martensite lath size in (I) as-built and (II) heat-treated arc-DED-PH13-8Mo, (III) as-built and (IV) heat-treated L-PBF-PH13-8Mo, evaluated from the EBSD results.

8Mo alloy. The strength increment due to the dislocation hardening is expressed as [40],

$$\Delta\sigma_d = 0.5MGb\sqrt{\rho_d} \quad (3)$$

where M is the Taylor factor and ρ_d is the dislocation density. The dislocation density in the L-PBF alloys could be 5 times higher than that in the arc-DED alloys [41,42]; the resulting dislocation hardening strength increment is 2.2 times higher in the L-PBF-PH13-8Mo. Considering these facts, the strength of the as-built L-PBF-PH13-8Mo is higher than the arc-DED counterpart.

The microstructural differences between the two alloys affected the physical properties as well. Both precipitation temperature range and precipitation activation energy were different in the two alloys. The lower precipitation activation energy in the L-PBF-PH13-8Mo (139 kJ/mol vs. 194 kJ/mol) could be due to the presence of the entangled dislocation networks (Fig. 15 (b)). The dislocations reduce the free energy barrier to nucleation by decreasing the total strain energy of the embryo [43]. However, unlike the previous studies where dislocations accelerated the precipitation kinetics in different alloying systems [43–46], the kinetics of precipitation in the L-PBF alloys is lower than that in the arc-DED alloy (Fig. 4), despite a higher dislocation density in the L-PBF alloy (compare Fig. 14 (b) and Fig. 15 (b)). Therefore, other microstructural differences, such as the residual δ-ferrite, different laths size, possible microsegregation, etc., are plausibly the determining factors in the kinetics of precipitation.

Direct aging of the AM-PH13-8Mo using the results of precipitation kinetics modeling (*i.e.* well-controlled aging conditions) resulted in breaking the strength-ductility trade-off in both alloys. However, it appears that the mechanism of such an achievement is different in the two alloys. Recalling the third strengthening mechanism in the PH stainless steels, *i.e.* precipitation hardening ($\Delta\sigma_p$), it is seen that the clusters in the arc-DED alloy and precipitates in the L-PBF alloy are playing a

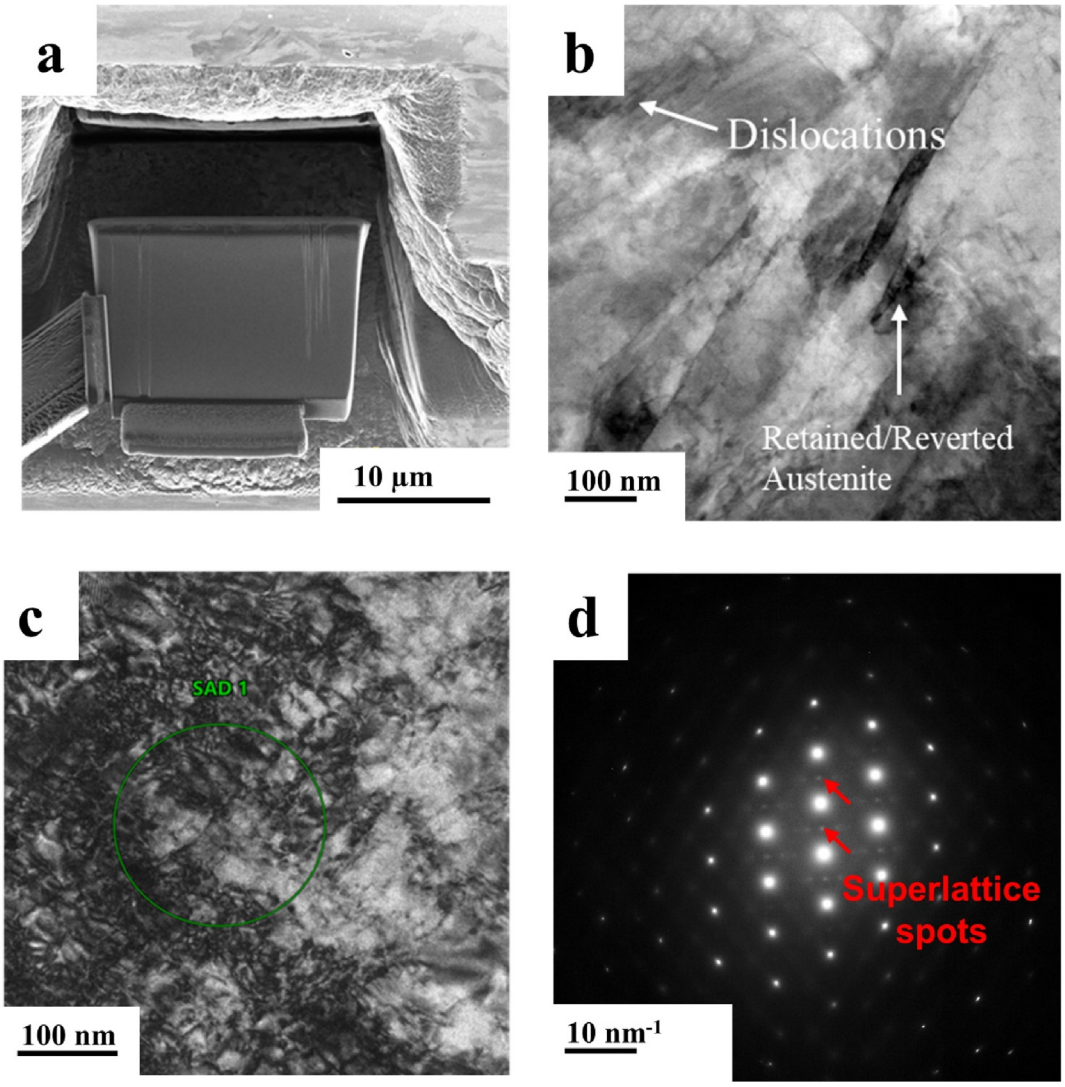

Fig. 14 – TEM study of DA-495-45: (a) Ion-milled trenches around a TEM sample prepared using the FIB method, (b) BF-STEM image showing dislocations and retained/reverted austenite, and (c) BF-TEM micrograph, and (d) SAED patterns of highlighted area in (c).

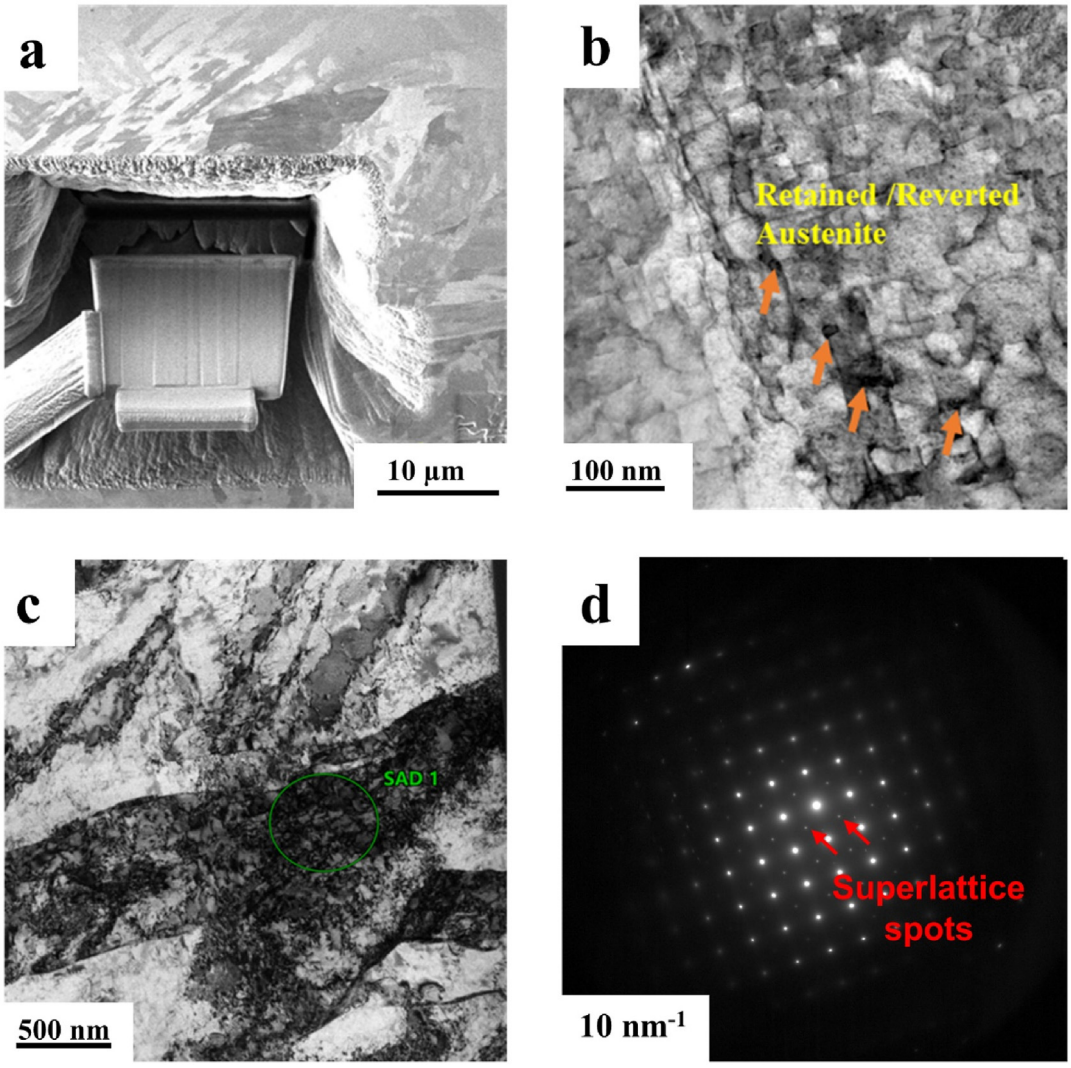

Fig. 15 – TEM study of DA-550-115: (a) Ion-milled trenches around a TEM sample prepared using the FIB method, (b) BF-STEM image with dislocations and retained/reverted austenite, and (c) BF-TEM micrograph, and (d) SAED patterns of highlighted area in (c).

major role in strength enhancement (Fig. 6). In the case of the evolution of β-NiAl, the precipitation hardening is governed by the particle cutting (shearing) mechanism [1,15,47]. Under the shearing mechanism, three factors contribute to the strength increment; order strengthening ($\Delta\sigma_o$), coherency strengthening ($\Delta\sigma_c$), and modulus mismatch strengthening ($\Delta\sigma_m$) [15,48]; *i.e.* $\Delta\sigma_p = \Delta\sigma_o + \Delta\sigma_c + \Delta\sigma_m$. As such, the strength increment due to the precipitation hardening in PH13–8Mo can be expressed as [1,15,48],

$$\Delta\sigma_p = \Delta\sigma_o + \Delta\sigma_c + \Delta\sigma_m = 0.4M\frac{\gamma_{APB}}{b}\left(\frac{3\pi f}{8}\right)^{1/2} + 2.6M(\varepsilon G)^{3/2}\left(\frac{2rf}{Gb}\right)^{1/2} + 0.0055M(\Delta G)^{\frac{3}{2}}\left(\frac{2f}{Gb^2}\right)^{\frac{1}{2}} b\left(\frac{r}{b}\right)^{\frac{3m}{2}-1} \quad (4)$$

where γ_{APB} is the anti-phase boundary (APB) energy of the β-NiAl, f is the volume fraction of β-NiAl, r is the mean radius of β-NiAl, ε is the lattice mismatch parameter, ΔG is the shear modulus mismatch between β-NiAl and matrix, and m is a constant. The evolution of clusters in the arc-DED alloy and precipitates in the L-PBF alloy resulted in different characteristics, which then altered some of the critical parameters in eq. (4), including γ_{APB}, f, r, ε, and ΔG. Therefore, the clusters in the arc-DED alloy and the precipitates in the L-PBF alloy are strengthening the material through distinct factors.

In addition to strength, the ductility improvement in the case of arc-DED and ductility retention in the case of L-PBF was controlled through two different mechanisms. Referring to Fig. 13, the austenite amount did not change during the heat treatment of the arc-DED alloy and negligibly changed during the heat treatment of the L-PBF alloy. Therefore, austenite is not playing a role in ductility level. It appears that the evolution of clusters in the arc-DED-PH13-8Mo is the responsible mechanism for the ductility improvement. As seen in Fig. 6,

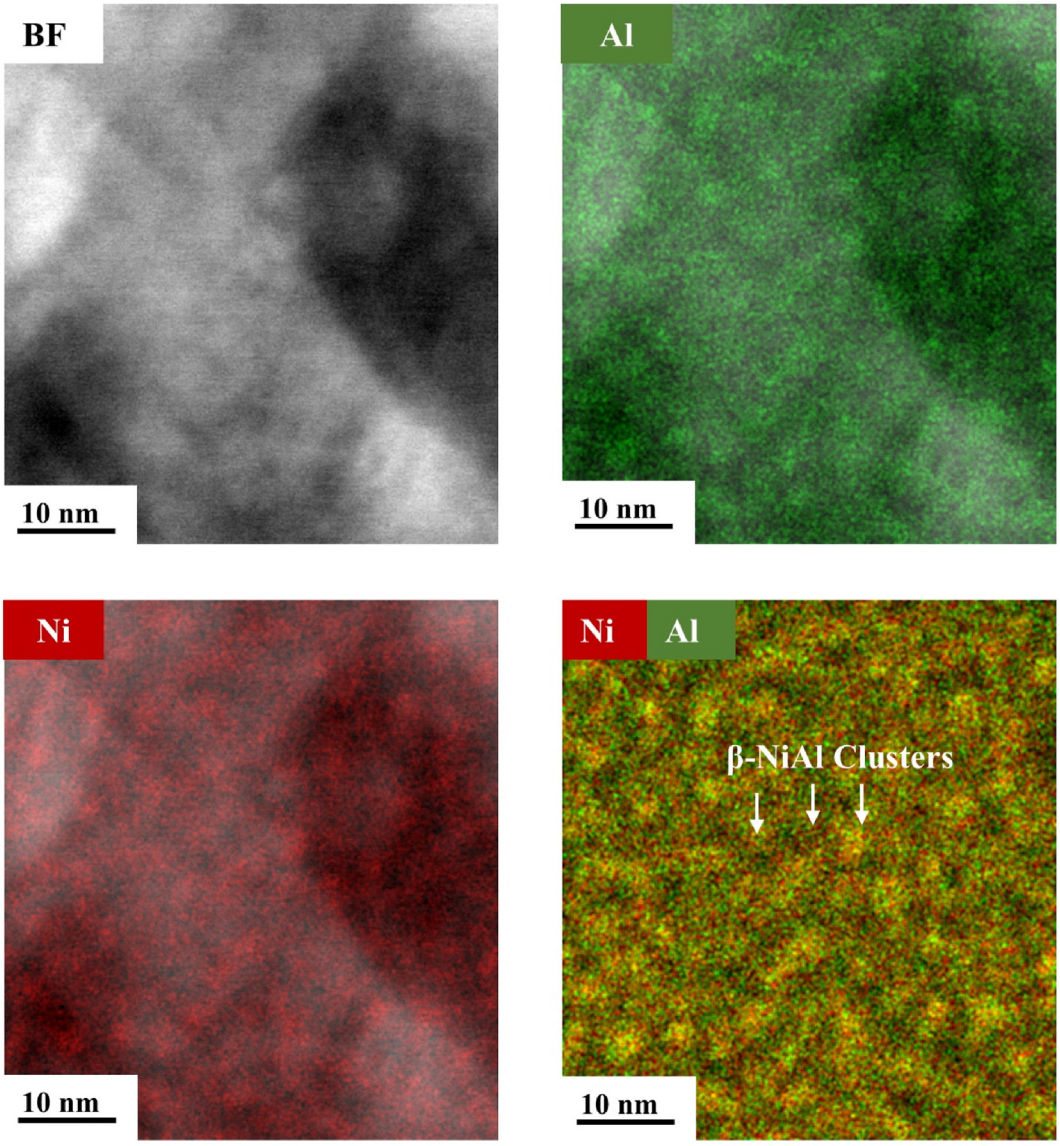

Fig. 16 – BF-STEM image along with the EDS elemental maps taken from DA-495-45 sample showing β-NiAl clusters.

the strain-hardening capability of arc-DED-PH13-8Mo (between YS and TS) significantly improved after the heat treatment, while such behavior is not observed in the L-PBF-PH13-8Mo. Such an improvement in the strain-hardening capability was a result of the evolution of the clusters. According to *Kim* et al. [49], the non-shearable nature of nano-scale precipitates accounts for high strain-hardening capability and ultrahigh strength achievement in steels. It appears that the shearability of the clusters is different than that of the precipitates, and therefore the ductility improved in the heat-treated arc-DED-PH13-8Mo. On the other hand, an ultrahigh level of strength was achieved in the heat-treated L-PBF-PH13-8Mo without any improvement in the strain-hardening capability. Therefore, the ductility retention mechanism in this material should be related to the entangled dislocations. As seen in Fig. 15 (b), the pre-existing dislocation networks were preserved during the aging heat treatment. These dislocation networks retain the ductility of the L-PBF-PH13-8Mo steel [21] since they increase the dislocation storage capability of the material [50]. The conventional heat treatment recipes include a high-temperature austenitization step (at 900–1010 °C), which is expected to annihilate the dislocation networks [15], consequently leading to ductility loss in the material. Nevertheless, it should be mentioned that the discussion of the current study is limited to the quasi-static properties. The fatigue properties need to be studied separately.

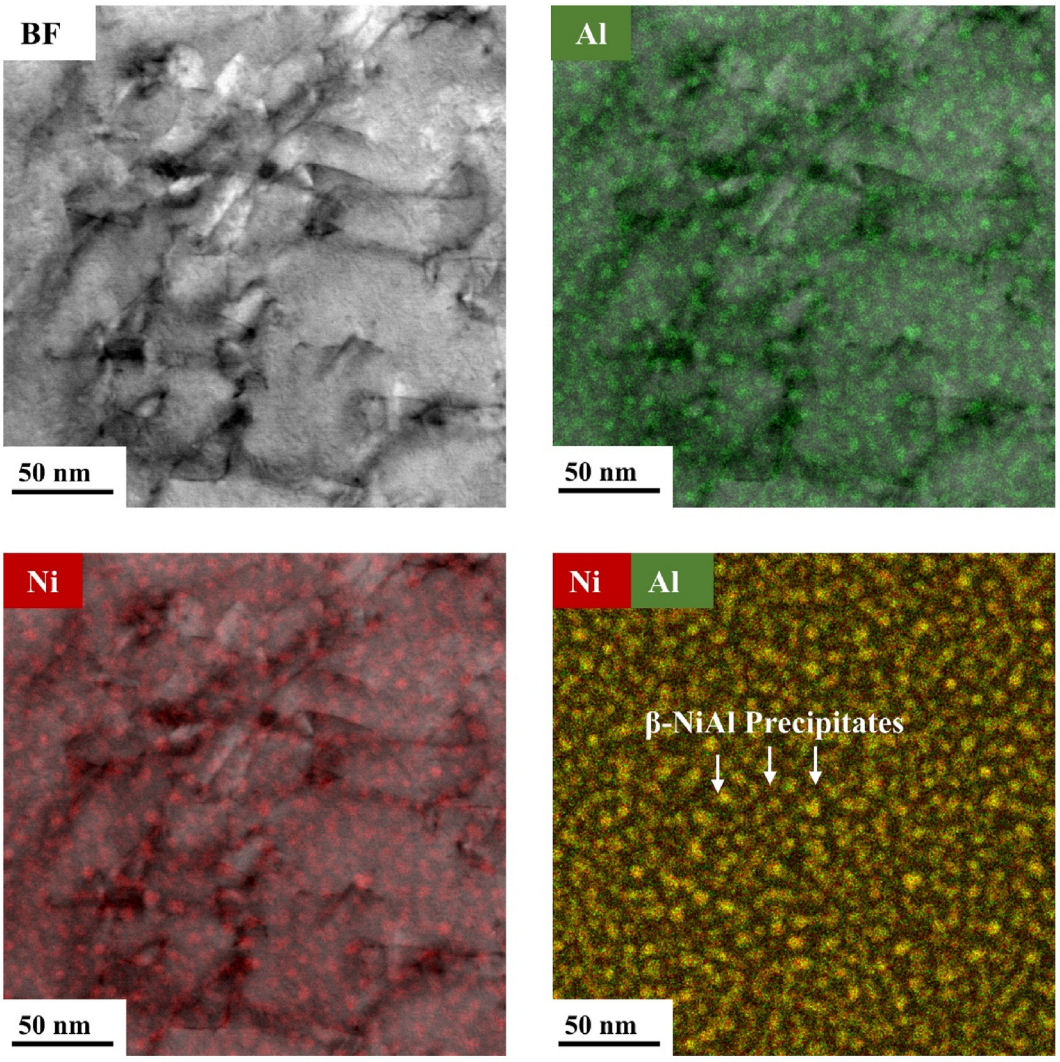

Fig. 17 – BF-STEM image along with the EDS elemental maps taken from DA-550-115 specimen showing β-NiAl precipitates.

5. Conclusions

In this study, the kinetics of precipitation phase transformation in AM-PH13-8Mo stainless steel fabricated through two different AM methods were investigated using DSC. The AM processes were arc-DED and L-PBF and the kinetics models were employed to design direct aging heat treatment recipes for each sample. The samples were then aged using the recommended recipes and their mechanical properties were evaluated. The mechanical properties were then correlated to the microstructural features at different length scales. The principal conclusions include.

- The microstructure of as-built samples exhibited substantial differences in terms of martensite lath size due to variations in their experienced cooling rates inherent to the nature of arc-DED and L-PBF processes. The arc-DED sample consisted of large columnar dendrites developed along the building direction, featured by residual δ-ferrite. In the L-PBF sample, ultrafine martensite laths developed in the material due to the rapid cooling conditions. The martensite lath size in the arc-DED-PH13-8Mo was an order of magnitude larger than that in the L-PBF counterpart.
- The DSC studies revealed that the kinetics of precipitation phase transformations are different in the two samples due to their different microstructures. Therefore, the recommended heat treatment recipes were different. In the case of arc-DED-PH13-8Mo, the recommended aging temperature and time were 495 °C and 45 min whereas for the L-PBF-PH13-8Mo the recommended temperature and time were 550 °C and 115 min.
- By employing the recommended heat treatment recipes, the strength and ductility improved concurrently in the arc-DED-PH13-8Mo sample as a result of the evolution of nano-scale β-NiAl clusters. The strain-hardening capability of the material was also enhanced significantly. It appears that the evolution of the clusters can evade the strength-ductility trade-off.
- In the case of L-PBF-PH13-8Mo, the recommended heat treatment recipe resulted in the evolution of nano-scale β-NiAl precipitates and enhancement of strength. The

ductility retention was a result of preserving the entangled pre-existing dislocation networks.
- This study provides important insight into the crucial role of processing history on the microstructure evolution and the resulting physical properties. The physical properties determine the kinetics of phase transformations, which have a great impact on the design of heat treatment and the resulting properties.

Data availability statement

The raw/processed data required to reproduce these findings cannot be shared at this time as the data also forms part of an ongoing study.

Declaration of competing interest

The authors declare that they have no known competing financial interests or personal relationships that could have appeared to influence the work reported in this paper.

Acknowledgment

The authors would like to acknowledge the Herff College of Engineering at the University of Memphis for the financial support of the research through the HCOE-FRG program. SKS and JK acknowledge support from the NSF DMREF program, award number 2119640.

REFERENCES

[1] Sun L, Simm TH, Martin TL, McAdam S, Galvin DR, Perkins KM, Bagot PAJ, Moody MP, Ooi SW, Hill P, Rawson MJ, Bhadeshia HKDH. A novel ultra-high strength maraging steel with balanced ductility and creep resistance achieved by nanoscale β-NiAl and Laves phase precipitates. Acta Mater 2018;149:285e301. https://doi.org/10.1016/j.actamat.2018.02.044.

[2] Liu P, Stigenberg AH, Nilsson JO. Quasicrystalline and crystalline precipitation during isothermal tempering in a 12Cr-9Ni-4Mo maraging stainless steel. Acta Metall Mater 1995;43(7):2881–90. https://doi.org/10.1016/0956-7151(94)00461-.

[3] Haghdadi N, Laleh M, Moyle M, Primig S. Additive manufacturing of steels: a review of achievements and challenges. J Mater Sci 2021;56:64–107. https://doi.org/10.1007/s10853-020-05109-0.

[4] Ping DH, Ohnuma M, Hirakawa Y, Kadoya Y, Hono K. Microstructural evolution in 13Cr-8Ni-2.5Mo-2Al martensitic precipitation-hardened stainless steel. Mater Sci Eng 2005;394:285–95. https://doi.org/10.1016/j.msea.2004.12.002.

[5] Hamlin RJ, DuPont JN. Microstructural evolution and mechanical properties of simulated heat-affected zones in cast precipitation-hardened stainless steels 17-4 and 13-8+Mo. Metall Mater Trans 2017;48:246–64. https://doi.org/10.1007/s11661-016-3851-6.

[6] Ghaffari M, Nemani AV, Nasiri A. Microstructure and mechanical behavior of PH 13–8Mo martensitic stainless steel fabricated by wire arc additive manufacturing. Addit Manuf 2022;49:102374. https://doi.org/10.1016/j.addma.2021.10237.

[7] Schnitzer R, Radis R, Nöhrer M, Schober M, Hochfellner R, Zinner S, Povoden-Karadeniz E, Kozeschnik E, Leitner H. Reverted austenite in PH 13-8 Mo maraging steels. Mater Chem Phys 2010;122:138–45. https://doi.org/10.1016/j.matchemphys.2010.02.058.

[8] Seetharaman V, Sundararaman M, Krishnan R. Precipitation hardening in a PH 13-8 Mo stainless steel. Mater Sci Eng 1981;47:1–11. https://doi.org/10.1016/0025-5416(81)90034-3.

[9] Leitner H, Schnitzer R, Schober M, Zinner S. Precipitate modification in PH13-8 Mo type maraging steel. Acta Mater 2011;59:5012–22. https://doi.org/10.1016/j.actamat.2011.04.053.

[10] Akita M, Uematsu Y, Kakiuchi T, Nakajima M, Kawaguchi R. Defect-dominated fatigue behavior in type 630 stainless steel fabricated by selective laser melting. Mater Sci Eng 2016;666:19–26. https://doi.org/10.1016/j.msea.2016.04.042.

[11] DebRoy T, Wei HL, Zuback JS, Mukherjee T, Elmer JW, Milewski JO, Beese AM, Wilson-Heid A, De A, Zhang W. Additive manufacturing of metallic components – process, structure and properties. Prog Mater Sci 2018;92:112–224. https://doi.org/10.1016/j.pmatsci.2017.10.001.

[12] Perez-Ruiz JD, de Lacalle LNL, Urbikain G, Pereira O, Martínez S, Bris J. On the relationship between cutting forces and anisotropy features in the milling of LPBF Inconel 718 for near net shape parts. Int J Mach Tool Manufact 2021;170:103801. https://doi.org/10.1016/j.ijmachtools.2021.103801.

[13] Perez-Ruiz JD, Marin F, Martínez S, Lamikiz A, Urbikain G, de Lacalle LNL. Stiffening near-net-shape functional parts of Inconel 718 LPBF considering material anisotropy and subsequent machining issues. Mech Syst Signal Process 2022;168:108675. https://doi.org/10.1016/j.ymssp.2021.108675.

[14] Nemani AV, Ghaffari M, Nasiri A. On the nucleation site and formation sequence of secondary phases during isothermal high-temperature aging of wire arc additively manufactured PH13–8Mo stainless steel. Vacuum 2022;201:111076. https://doi.org/10.1016/j.vacuum.2022.111076.

[15] Hadadzadeh A, Shahriari A, Amirkhiz BS, Li J, Mohammadi M. Additive manufacturing of an Fe–Cr–Ni–Al maraging stainless steel: microstructure evolution, heat treatment, and strengthening mechanisms. Mater Sci Eng, A 2020;787:139470. https://doi.org/10.1016/j.msea.2020.139470.

[16] Rafieazad M, Ghaffari M, Vahedi Nemani A, Nasiri A. Microstructural evolution and mechanical properties of a low-carbon low-alloy steel produced by wire arc additive manufacturing. Int J Adv Manuf Technol 2019;105:2121–34. https://doi.org/10.1007/s00170-019-04393-8.

[17] Xia C, Pan Z, Polden J, Li H, Xu Y, Chen S, Zhang Y. A review on wire arc additive manufacturing: monitoring, control and a framework of automated system. J Manuf Syst 2020;57:31–45. https://doi.org/10.1016/j.jmsy.2020.08.008.

[18] Fabian R, Hadadzadeh A. Breaking strength-ductility trade-off in laser-powder bed fused Fe–Cr–Ni–Al maraging stainless steel: controlled precipitation and preserved dislocations. Mater Sci Eng, A 2023;868:144761. https://doi.org/10.1016/j.msea.2023.144761.

[19] EOS, GmbH—Electro Optical Systems. Material data sheet: EOS stainless steel CX. München; 2022. www.eos.info.

[20] Ghaffari M, Nemani AV, Nasiri A. Microstructural evolution and mechanical performance after precipitation hardening of PH 13-8Mo martensitic stainless steel fabricated by wire

arc additive manufacturing. Materialia 2022;24:101507. https://doi.org/10.1016/j.mtla.2022.101507.
[21] Liu L, Ding Q, Zhong Y, Zou J, Wu J, Chiu YL, Li J, Zhang Z, Yu Q, Shen Z. Dislocation network in additive manufactured steel breaks strength–ductility trade-off. Mater Today 2018;21:354–61. https://doi.org/10.1016/j.mattod.2017.11.004.
[22] Marin F, de Souza AF, Mikowski A, Henrique L, Fontanella G, Soares P, de Lacalle LL. Energy density effect on the interface zone in parts manufactured by laser powder bed fusion on machined bases. Int. J. of Precis. Eng. and Manuf.-Green Tech. 2022. https://doi.org/10.1007/s40684-022-00470-8.
[23] Pascual A, Ortega N, Plaza S, de Lacalle LNL, Ukar E. Analysis of the influence of L-PBF porosity on the mechanical behavior of AlSi10Mg by XRCT-based FEM. J Mater Res Technol 2023;22:958–81. https://doi.org/10.1016/j.jmrt.2022.11.172.
[24] Technical data sheets & safety data sheets – iron base alloys – US welding corporation, (n.d.), https://www.usweldingcorp.net/technical-data/tds-sds-iron-basealloys/(accessed December 15, 2021).
[25] Asgari H, Mohammadi M. Microstructure and mechanical properties of stainless steel CX manufactured by Direct Metal Laser Sintering. Mater Sci Eng 2018;709:82–9. https://doi.org/10.1016/j.msea.2017.10.045.
[26] Haghshenas M, Klassen RJ. Assessment of the depth dependence of the indentation stress during constant strain rate nanoindentation of 70/30 brass. Mater Sci Eng, A 2013;572:91–7. https://doi.org/10.1016/j.msea.2013.02.009.
[27] Shakil SI, Zoeram AS, Pirgazi H, Shalchi-Amirkhiz B, Poorganji B, Mohammadi M, Haghshenas M. Microstructural-micromechanical correlation in an Al–Cu–Mg–Ag–TiB2 (A205) alloy: additively manufactured and cast. Mater Sci Eng, A 2022;832:142453. https://doi.org/10.1016/j.msea.2021.142453.
[28] Leyland A, Matthews A. On the significance of the H/E ratio in wear control: a nanocomposite coating approach to optimised tribological behaviour. Wear 2000;246:1–11. https://doi.org/10.1016/S0043-1648(00)00488-9.
[29] Lin J, Moore JJ, Mishra B, Pinkas M, Sproul WD. The structure and mechanical and tribological properties of TiBCN nanocomposite coatings. Acta Mater 2010;58:1554–64. https://doi.org/10.1016/j.actamat.2009.10.063.
[30] Ehtemam-Haghighi S, Cao G, Zhang LC. Nanoindentation study of mechanical properties of Ti based alloys with Fe and Ta additions. J. Alloys Compnd. 2017;692:892–7. https://doi.org/10.1016/j.jallcom.2016.09.123.
[31] Cheng YT, Cheng CM. Relationships between hardness, elastic modulus, and the work of indentation. Appl Phys Lett 1998;73:614–6. https://doi.org/10.1063/1.121873.
[32] Basak A, Das S. Epitaxy and microstructure evolution in metal additive manufacturing. Annu Rev Mater Res 2016;46:125–49. https://doi.org/10.1146/annurev-matsci070115-031728.
[33] Herzog D, Seyda V, Wycisk E, Emmelmann C. Additive manufacturing of metals. Acta Mater 2016;117:371–92. https://doi.org/10.1016/j.actamat.2016.07.019.
[34] Sanjari M, Mahmoudiniya M, Pirgazi H, Tamimi S, Ghoncheh MH, Shahriairi A, Hadadzadeh A, Amirkhiz BS, Purdy M, de Araujo EG, Kestens L, Mohammadi M. Microstructure, texture, and anisotropic mechanical behavior of selective laser melted maraging stainless steels. Mater Char 2022;192:112185. https://doi.org/10.1016/j.matchar.2022.112185.
[35] Brooks JA, Garrison WM. Weld microstructure development and properties of precipitation-strengthened martensitic stainless steels. Weld J 1999;78:280–91.
[36] Lippold JC, Kotecki DJ. Precipitation-hardening stainless steels. New Jersey: Weld. Metall. Weldability Stainl. Steels; 2005. p. 264–86.
[37] Guo Z, Sha W, Li D. Quantification of phase transformation kinetics of 18 wt.% Ni C250 maraging steel. Mater Sci Eng 2004;373:10–20. https://doi.org/10.1016/j.msea.2004.01.040.
[38] Antonysamy AA. Microstructure, texture and mechanical property evolution during additive manufacturing of Ti6Al4V alloy for aerospace applications. Manchester (UK): The University of Manchester; 2012.
[39] Wang YM, Voisin T, McKeown JT, Ye J, Calta NP, Li Z, Zeng Z, Zhang Y, Chen W, Roehling TT, Ott RT, Santala MK, Depond PJ, Matthews MJ, Hamza AV, Zhu T. Additively manufactured hierarchical stainless steels with high strength and ductility. Nat Mater 2018;17:63–70. https://doi.org/10.1038/NMAT5021.
[40] Abe F. Precipitate design for creep strengthening of 9% Cr tempered martensitic steel for ultra-supercritical power plants. Sci Technol Adv Mater 2008;9(1):013002. https://doi.org/10.1088/1468-6996/9/1/013002.
[41] Pesicka J, Aghajani A, Somsen C, Hartmaier A, Eggeler G. How dislocation substructures evolve during long-term creep of a 12% Cr tempered martensitic ferritic steel. Scripta Mater 2010;62:353–6. https://doi.org/10.1016/j.scriptamat.2009.10.037.
[42] Bertsch KM, Meric de Bellefon G, Kuehl B, Thoma DJ. Origin of dislocation structures in an additively manufactured austenitic stainless steel 316L. Acta Mater 2020;199:19–33. https://doi.org/10.1016/j.actamat.2020.07.063.
[43] Yan J, Hodge AM. Study of β precipitation and layer structure formation in Al 5083: the role of dispersoids and grain boundaries. J Alloys Compd 2017;703:242–50. https://doi.org/10.1016/j.jallcom.2017.01.360.
[44] Wang SS, Jiang JT, Fan GH, Panindre AM, Frankel GS, Zhen L. Accelerated precipitation and growth of phases in an Al-Zn-Mg-Cu alloy processed by surface abrasion. Acta Mater 2017;131:233–45. https://doi.org/10.1016/j.actamat.2017.03.074.
[45] Doremus RH. The role of dislocations in carbide precipitation in α-Iron. Acta Metall 1958;6:674–9. https://doi.org/10.1016/0001-6160(58)90058-0.
[46] Love GR. Dislocation pipe diffusion. Acta Metall 1964;12:731–7. https://doi.org/10.1016/0001-6160(64)90220-2.
[47] Gladman T. Precipitation hardening in metals. Mater Sci Technol 1999;15(1):30–6. https://doi.org/10.1179/026708399773002782.
[48] Seidman DN, Marquis EA, Dunand DC. Precipitation strengthening at ambient and elevated temperatures of heat-treatable Al(Sc) alloys. Acta Mater 2002;50:4021–35. https://doi.org/10.1016/S1359-6454(02)00201-X.
[49] Kim SH, Kim H, Kim NJ. Brittle intermetallic compound makes ultrastrong lowdensity steel with large ductility. Nature 2015;518:77–9. https://doi.org/10.1038/nature14144.
[50] Liu J, Jin Y, Fang X, Chen C, Feng Q, Liu X, Chen Y, Suo T, Zhao F, Huang T, Wang H, Wang X, Fang Y, Wei Y, Meng L, Lu J, Yang W. Dislocation strengthening without ductility trade-off in metastable austenitic steels. Sci Rep 2016;6:35345. https://doi.org/10.1038/srep35345.